Tuning the Excitonic States in MoS_2/Graphene van der Waals Heterostructures via Electrochemical Gating

Yang Li, Cheng-Yan Xu, Jing-Kai Qin, Wei Feng, Jia-Ying Wang, Siqi Zhang, Lai-Peng Ma, Jian Cao, Ping An Hu, Wencai Ren, and Liang Zhen**

The behavior of excitons in van der Waals (vdWs) heterostructures depends on electron–electron interactions and charge transfer at the hetero-interface. However, what still remains to be unraveled is to which extent the carrier densities of both counterparts and the band alignment in the vdWs heterostructures determine the photoluminescence properties. Here, we systematically study the photoluminescence properties of monolayer MoS_2/graphene heterostructures by modulating the carrier densities and contact barrier at the interface via electrochemical gating. It is shown that the PL intensities of excitons can be tuned by more than two orders of magnitude, and a blue-shift of the exciton peak of up to 40 meV is observed. By extracting the carrier density of MoS_2 using an electric potential distribution model, and the Schottky barrier using first-principle calculations, we find that the controllable carrier density in MoS_2 plays a dominant role in the PL tuning at negative gate bias, whereas the interlayer relaxation of excitons induced by the Schottky barrier has a major contribution at positive gate bias. This is further verified by controlling the tunneling barrier and screening field across MoS_2 by inserting self-assembled monolayers (SAMs) at the interface. These findings will benefit to better understand the effect of many-body interactions and hetero-interfaces on the optical and optoelectronic properties in vdWs heterostructures.

1. Introduction

Atomically thin transition metal dichalcogenides (TMDs) have been considered to be attractive candidates for optoelectronic and valleytronic applications because of their unique electronic and optical properties, such as strong light–matter interactions, spin–orbit coupling, and coupled spin–valley degree.[1–8] Because of their large in-plane effective mass, the electron–electron and electron–hole interactions in monolayer TMDs are expected to play an important role in the formation of many-body bound quasiparticles, such as neutral and charged excitons, which determines the electronic transport and optical transition in monolayer TMDs. Until now, most relevant research on the tunability of excitonic states has been focused on monolayer TMDs, such as MoS_2, WSe_2, and $MoSe_2$, where the behavior of the excitons can be modulated by controlling the carrier density through chemical and electrical doping methods, as well as by changing the energy band structures by strain engineering, dielectric screening, or alloying.[9–16]

As an emerging class of materials, van der Waals (vdWs) heterostructures stacked with several two-dimensional materials, such as graphene, BN, or TMDs by van der Waals interaction, have presented some fascinating new phenomena induced by quantum coupling.[17–24] Looking at the exciton behavior in vdWs heterostructures, on the one hand, we can see that the potential electronic coupling in vdWs heterostructures will make it possible to change the electron–electron or electron–hole interactions, further enriching the behavior of many-body bound quasiparticles.[23,25–28] On the other hand, the high-quality hetero-interface without dangling bonds, which is characteristic for van der Waals heterostructures, is advantageous to tailor the intrinsic

Y. Li, Prof. C. Y. Xu, Prof. J. Cao
State Key Laboratory of Advanced Welding and Joining
Harbin Institute of Technology
Harbin 150001, P. R. China
E-mail: cy_xu@hit.edu.cn

Y. Li, Prof. C. Y. Xu, J. K. Qin, W. Feng, J. Y. Wang, Prof. L. Zhen
School of Materials Science and Engineering
Harbin Institute of Technology
Harbin 150001, P. R. China
E-mail: lzhen@hit.edu.cn

Prof. P. A. Hu, Prof. L. Zhen
Micro/Nano Technology Research Center
Harbin Institute of Technology
Harbin 150080, P. R. China

Dr. S. Q. Zhang
Department of Physics
Harbin Institute of Technology
Harbin 150001, P. R. China

Prof. L. P. Ma, Prof. W. C. Ren
Shenyang National Laboratory for Materials Science
Institute of Metal Research
Chinese Academy of Sciences
Shenyang 110016, P. R. China

DOI: 10.1002/adfm.201503131

electronic and optical properties of TMDs, as the built-in electric field strongly affects the charge transfer and dissociation of excitons.[19,29–31] Very recently, a few groups have studied the behavior of excitons in TMD/TMD heterostructures with type-II band alignment, such as WSe_2/MoS_2, MoS_2/WS_2, and $MoSe_2/WSe_2$, and experimentally unveiled the fast charge transfer of the photogenerated holes, the interlayer relaxation induced photoluminescence (PL) quenching, and the long-lived interlayer exciton.[19,31–34] Nevertheless, tailoring both the electronic structure and hetero-interface for tuning the excitonic states in TMD vdWs heterostructures has not been carried out until now. Unlike TMD/TMD heterostructures, the weak van der Waals interlayer coupling in TMD/graphene heterostructures contributes to the unchanged electronic states of participating materials.[26,34,35] From first-principle calculations, the interaction around the Γ point in all TMD/graphene heterostructures is negligible, and the electronic structure resembles that of two independent monolayers.[26] Moreover, by using angle-resolved photoemission spectroscopy, Diaz et al. were able to report that the Dirac cone of graphene remained intact and no significant charge-transfer doping was detected between MoS_2 and graphene.[35] Moreover, the large tunability of the graphene Fermi level and the stable excitonic states of the MoS_2 monolayer (neutral excitons and negative trions) at room temperature make MoS_2/graphene heterostructures an ideal platform to unveil the problems aforementioned.[5,9,36,37] A recently reported related work showed that MoS_2/graphene heterostructures could be used for ultrasensitive DNA detection by monitoring the change of excitonic states in MoS_2 through the charge transfer at the hetero-interface.[38] Therefore, explicitly studying the excitonic behavior in MoS_2/graphene heterostructures, and then discerning the dominant factor that determines the photoluminescence behavior will be beneficial to the exploitation of new-concept and highly efficient optoelectronic applications.

Here, we systematically studied the dependence of the photoluminescence property of monolayer MoS_2/graphene heterostructures on the carrier density of MoS_2 as well as the band alignment at the interface via electrochemical gating. It is shown that the integrated excitons intensities could be modulated by more than two orders of magnitude (>200). Moreover, the trion/exciton intensity ratio (I_{A^-}/I_A) could be tuned by up to 30 times, and a blue-shift of the excitons of up to 40 meV was observed. The large tunability of the MoS_2 carrier density played a dominant role on the PL modulation at negative gate bias, whereas the exciton splitting driven by the built-in electric field at the Schottky contact had a major contribution at positive gate bias. Furthermore, by controlling both the electric-field screening and contact barrier at the hetero-interface by inserting insulating SAMs with different thickness at the MoS_2/graphene interface, the weak dependence of the PL in MoS_2/SAMs/graphene heterostructures at gate bias also verified the impact of the hetero-interface on the PL tuning in the MoS_2/graphene system.

2. Results and Discussion

Figure 1a shows the schematic illustration of the monolayer MoS_2/graphene device used in our experiments. A monolayer of MoS_2 was first mechanically exfoliated onto a Si/SiO_2 substrate, and subsequently stacked with a monolayer of chemical vapor deposition (CVD)-graphene, and then a gel-like solid electrolyte ($LiClO_4$ and polyethylene oxide (PEO) dissolved in methane with a ratio of 0.012:0.1:4) was used as the top-gate dielectric. Details of the samples and devices fabrication can be found in the Experimental Section. The Raman and PL signals of the MoS_2/graphene heterostructures as a function of gate bias were collected by Raman spectroscopy. A typical optical microscopy image of the device is shown in Figure 1b, where the insets present the atomic force microscopy (AFM) topography and height profile of the MoS_2 monolayer with a thickness of around 0.9 nm. The characteristics of the MoS_2 monolayer were further verified by Raman and PL spectra, as shown in Figure 1c. The peak distance between the $E_{2g}{}^1$ and A_{1g} modes of the MoS_2 monolayer was 18.2 cm^{-1}. It should be noted that compared to the separate MoS_2 monolayer (shown in Figure S1 in the Supporting Information), the out-of-plane mode A_{1g} presents a redshift of about 2 cm^{-1}, which results from the interlayer interaction between graphene and MoS_2.[29,38,39] Moreover, the Raman spectrum in Figure 1c shows the prominent features of graphene, namely the Raman G-band at 1577 cm^{-1} and the 2D-band at 2694 cm^{-1}, and a FWHM of 30 cm^{-1} was found for the Raman 2D peak, which matches the characteristics of a graphene monolayer..[27,34] The PL spectra of the monolayer MoS_2/graphene heterostructure and the separate MoS_2 on a Si/SiO_2 substrate are presented in Figure 1d. Compared to the separate MoS_2 layer, the PL peak of the heterostructure presents a slight blue-shift and the PL intensity is partially quenched by about 45%, which can be attributed to the exciton splitting by the built-in electric field at the MoS_2/graphene interface.[29,30] Specifically, due to the Schottky barrier at the interface, the photogenerated holes are injected from the valence band of MoS_2 to graphene, whereas the photogenerated electrons in the conductance band of MoS_2 are prohibited to diffuse to graphene because of the built-in barrier formed at the hetero-interface. Therefore, the exciton recombination efficiency and the resultant PL intensity of MoS_2/graphene significantly decreased. It should be noted that the multiple sharp peaks in the PL spectra originated from the Raman vibrational modes of graphene and the electrolyte gels (see assignments of these peaks in Figure 1c).

As is schematically illustrated in Figure 1a, a negative gate bias is applied between the gel and the Au electrode, and the PL spectra of MoS_2/graphene at a gate bias of 0 to −3.6 V are presented in **Figure 2**a. It is evident that with increasing negative gate bias (V_g), the absolute PL intensity increased significantly and the PL peak narrowed accordingly. The peak maximum showed a blue-shift of about 20 nm (ca. 35 meV). The PL spectra of the MoS_2/graphene heterostructure at a gate bias from 0 to 2 V are shown in Figure 2b. In contrast to the case at negative bias ($V_g < 0$), the absolute PL intensity decreased rapidly with increasing gate bias at $V_g > 0$, and was almost totally quenched at a gate bias of 2 V. The absolute PL intensity was thus reversibly tunable over a large range of more than 100 times in the gate bias range from -3.6 to 2 V, which is much higher than that reported previously.[9,10,38] Due to the strong spin–orbit interactions of the MoS_2 monolayer and the interplay between a neutral exciton and an excessive electron,

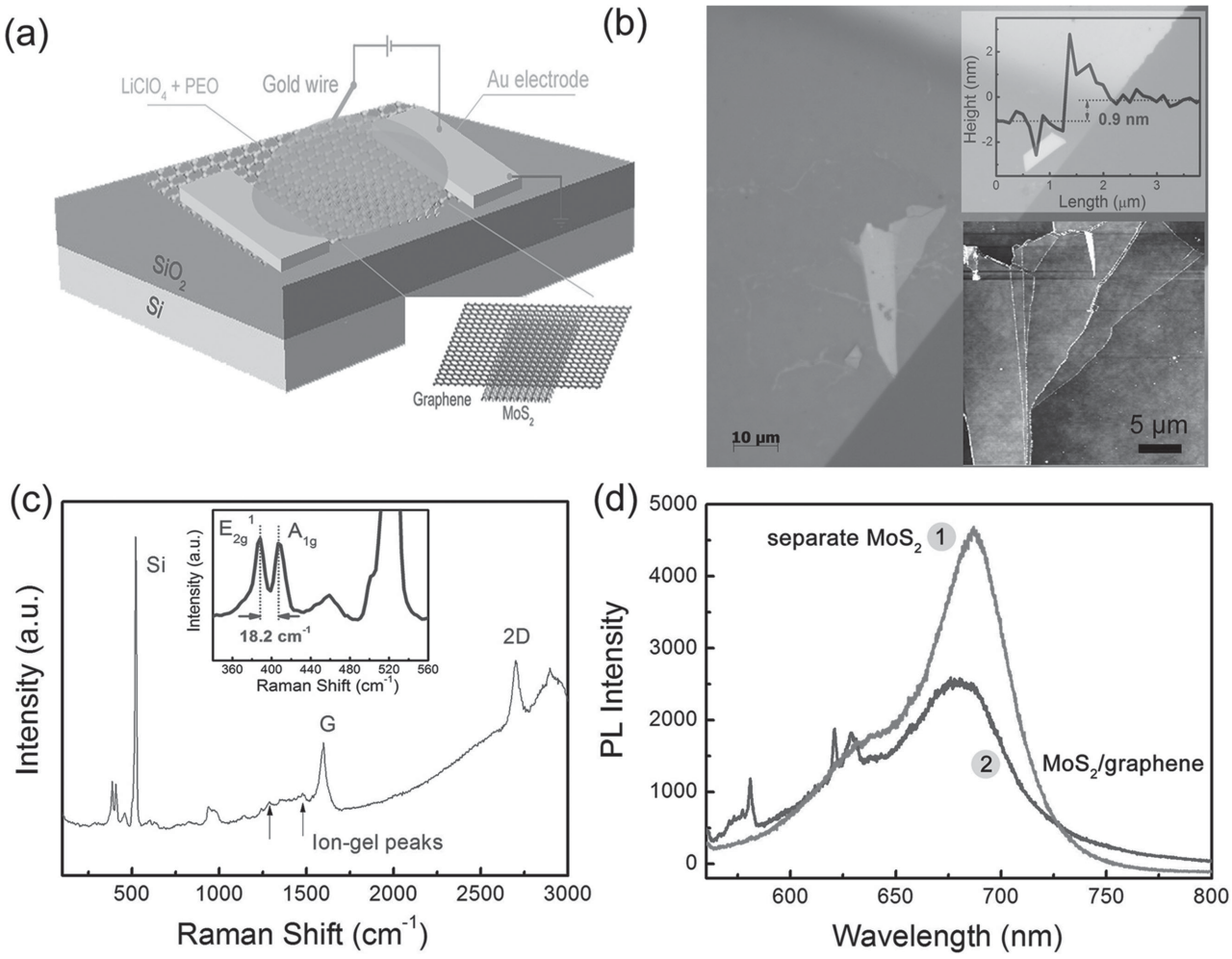

Figure 1. a) Schematic illustration of the MoS_2/graphene device. A mechanically exfoliated MoS_2 monolayer is stacked with CVD-grown graphene, and then the MoS_2/graphene device is fabricated with an ion-gel top dielectric for Raman and PL spectra measurements. b) Optical microscopy image of the MoS_2/graphene device on a Si/SiO_2 substrate. The insets show the AFM topography and corresponding height profile of the MoS_2 monolayer with a thickness of around 0.9 nm. c) Raman spectrum of MoS_2/graphene covered with ion-gel. The inset presents the enlarged Raman spectrum, showing the $E_{2g}{}^1$ and A_{1g} Raman modes of the MoS_2 monolayer, and the peak distance between $E_{2g}{}^1$ and A_{1g} is 18.2 cm^{-1}. d) The PL spectra of the MoS_2/graphene heterostructure covered with ion-gel and of a separate MoS_2 monolayer on a Si/SiO_2 substrate.

there are three stable excitons in the MoS_2 monolayer, namely, the A exciton, the B exciton, and the A^- trion.[5,9] In Figure 2c, the typical PL spectra of the MoS_2/graphene heterostructure at a gate bias of 0.9, 0, –2.1, and –3.6 V were fitted with three Lorentzian peaks, corresponding to the three excitonic states of the A exciton (1.86 eV), A^- trion (1.80 eV), and B exciton (1.96 eV). The intensity of the A^- trion is comparable to that of the A exciton at $V_g = 0$. The strong radiative recombination of trions in MoS_2 is consistent with previous results.[9,11] The PL property of the MoS_2 monolayer at a gate bias of –3.6 V was totally dominated by the A exciton, suggesting that the excitons recombined without forming trions because of the decrease in the number of excess electrons in MoS_2.

Subsequently, we monitored the evolution of the excitonic states of MoS_2/graphene at different gate bias. The peak positions of the A, A^-, and B excitons, and integrated intensities of A and A^- as a function of gate bias are plotted in **Figure 3**a,b, respectively. From Figure 3a, it can be seen that the energy positions of all three peaks increased at both negative and positive bias,, and the maximum shifts of the A, A^-, and B excitons were determined to be 10, 35, and 40 meV, respectively. As shown in Figure 3b, the PL intensities of both the neutral exciton (A) and ($A+A^-$) increased almost exponentially as a function of the gate bias and could be modulated by more than two orders of magnitude (> 200). The intensity of the A^- trion peak was quenched by more than 20 times at positive gate biases from 0 to 2 V, whereas it presented only slight variations at negative bias from 0 to –2.1 V.

The trion binding energy, ε_{A^-}, is the energy required for removal of one electron from the trion, which is calculated by the energy difference between the A exciton and the A^- trion. The dependence of ε_{A^-} on the gate bias is shown in Figure 3c. The trion binding energy (ε_{A^-}) decreased gradually regardless of whether a negative or positive gate bias was applied. The trion PL spectra weight, which is defined by the intensity ratio of trions and excitons (I_{A^-}/I_A), also changed with gate bias. As shown in Figure 3d, I_{A^-}/I_A decreased from about 3 to 0.1 with

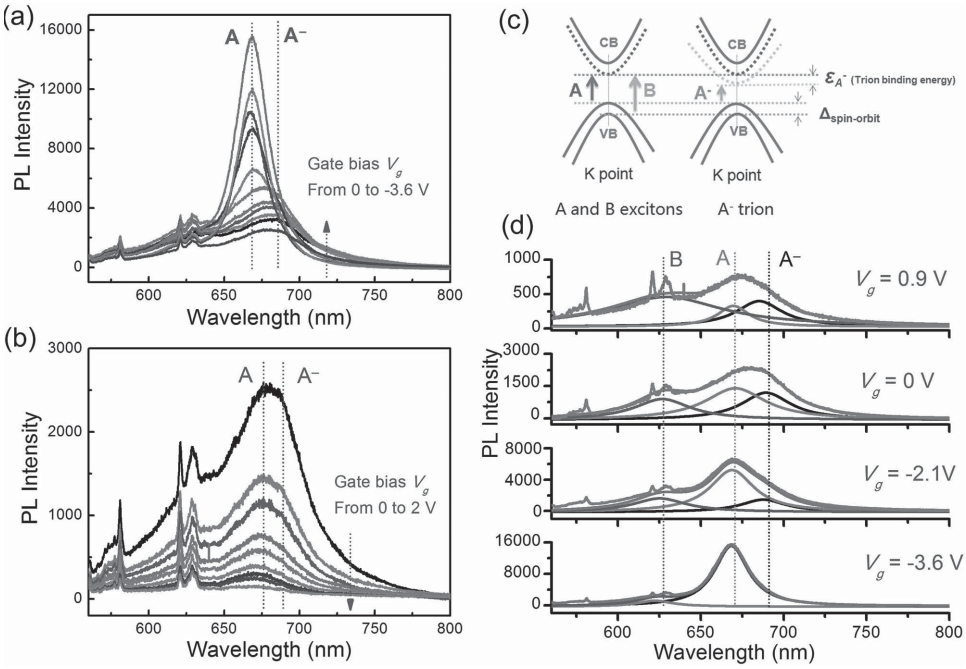

Figure 2. a,b) Photoluminescence spectra of the MoS_2/graphene heterostructure at negative gate bias from 0 to –3.6 V, and positive gate bias from 0 to 2 V, respectively. c) Top: Schematics of the exciton and trion quasi-particles and transitions at the *K* point in the Brillioun zone. Δ and ε_{A^-} denote the valence band splitting and trion binding energy, respectively. Bottom: Typical PL spectra of MoS_2/graphene fitted by three Lorenztian peaks, corresponding to the A exciton (1.86 eV), B exciton (1.96 eV), and A^- trion (1.80 eV), at gate biases of 0.9, 0, –2.1, and –3.6 V.

changing gate bias from 0 to –3.6 V, whereas it decreased slightly when $V_g > 0$. In the steady state, the A^-/A intensity ratio can be expressed as

$$\frac{I_{A^-}}{I_A} = \frac{\Gamma_{A^-} N_{A^-}}{\Gamma_A N_A} \quad (1)$$

where N_A and N_{A^-} are the exciton and trion concentrations, respectively; and Γ_A Γ_{A^-} represent the radiative recombination rates of the excitons and trions, respectively.[10,16,28] Radiative recombinations occur mainly at the K point of the Brillouin zone. The mass action law has been used before to relate the

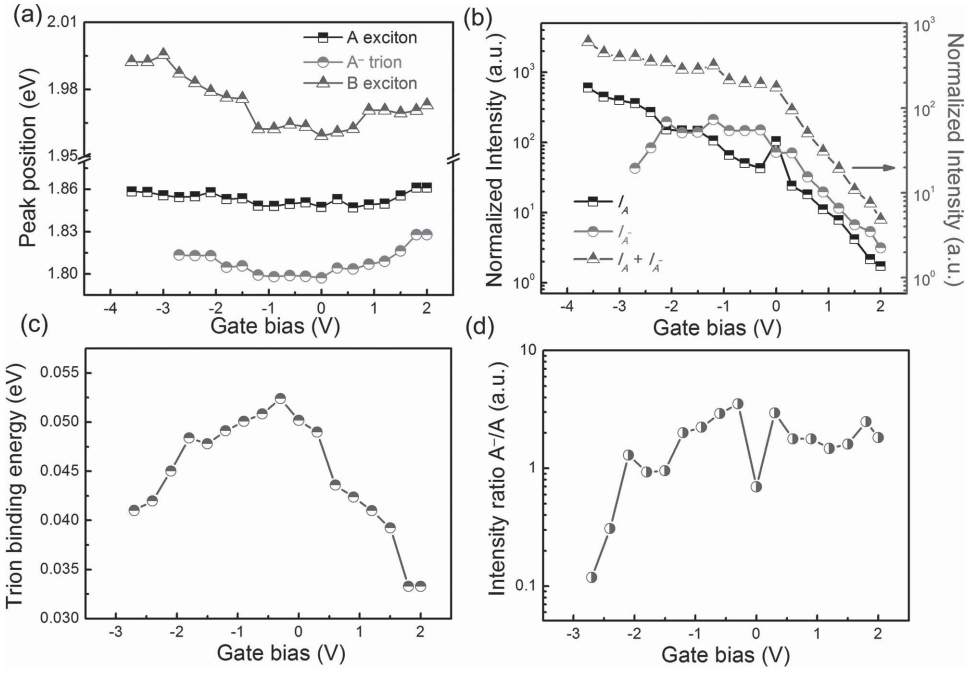

Figure 3. Gate bias dependence of: a) bo PL peak positions of A, B, and A^-, b) PL intensities of A, A^-, and (A+A^-), c) trion binding energy ε_{A^-}, d) A^- trion to A exciton PL intensity ratio (I_{A^-}/I_A).

concentrations of the neutral exciton, excess electron, and hole to the dynamics of the formation of neutral and charged excitons in a two-dimensional electron gas system (quantum wells) or two-dimensional semiconductor materials and heterostructures. Therefore, the ratio of the A^- and A concentrations can be expressed similar to those in the steady state as[10,16,28,40]

$$\frac{N_{A^-}}{N_A} = \frac{\pi\hbar^2 n_e M_{A^-}}{4 M_A m_e k_B T} \exp\left(\frac{\varepsilon_{A^-}}{k_B T}\right) \quad (2)$$

where n_e, ε_{A^-}, and m_e are the excess electron concentration, trion binding energy, and electro-effective mass, respectively; M_A and M_{A^-} are the effective masses of the exciton and trion, respectively. Therefore, the A^-/A intensity ratio can be finally expressed as

$$\frac{I_{A^-}}{I_A} \propto n_e \frac{M_{A^-}}{M_A m_e} \exp\left(\frac{\varepsilon_{A^-}}{k_B T}\right) \quad (3)$$

Equation (3) indicates that there are two main contributions to the A^-/A intensity ratio: the excess carrier density, n_e, and the trion binding energy, ε_{A^-}. To quantitatively reveal the contribution of each factor in the above equation to the change of the A^-/A intensity ratio with gate bias, we tried to exact the amplitude of the change in $\exp(\varepsilon_{A^-}/k_B T)$ and $n_e[M_{A^-}/(M_A m_e)]$, corresponding to the trion binding energy and excess electron concentration. When $V_g < 0$, I_{A^-}/I_A increases from 0.1 to about 3 (or from 1 to 30), and $\exp(\varepsilon_{A^-}/k_B T)$ increased from 4.93 to 7.64 (or from 1 to 1.55; ε_{A^-} was obtained from Figure 3c). Obviously, $n_e[M_{A^-}/(M_A m_e)]$, that is the excess electron concentration, was the major contribution term to the variation in I_{A^-}/I_A, whereas the $\exp(\varepsilon_{A^-}/k_B T)$ had only a more modest contribution to the A^-/A intensity ratio. On the other hand, when $V_g > 0$, I_{A^-}/I_A decreased from 3 to about 2 (or from 1.5 to 1), and $\exp(\varepsilon_{A^-}/k_B T)$ decreased from 7.44 to 3.56 (or from 2.09 to 1), indicating that the $\exp(\varepsilon_{A^-}/k_B T)$, that is the variation in the trion binding energy, was the major contributor to the variation in I_{A^-}/I_A.

Lin et al. reported the effect of the dielectric constant of the environment on the photoluminescence properties of MoS_2 monolayers and a variation in the exciton or trion PL peak positions and intensities was observed.[16] Can the PL variation in MoS_2/graphene be attributed to the dielectric screening effect of graphene? Santos et al. studied the effect of the out-of-plane electric field on the effective dielectric constant in graphene, and found that for monolayered graphene the dielectric constant varied slightly (ε around 3) when the electric field approached 1 V/Å (corresponding to V_g of 5 V in our experiment).[41] Therefore, we can exclude the possibility that the dielectric screening of graphene has a major effect on the PL modulation in the heterostructure.

To further understand the origin of the variation in the photoluminescence properties of the MoS_2/graphene heterostructures, we tried to extract the carrier densities of both graphene and MoS_2. Firstly, according to the Raman spectra shown in Figure S2 (Supporting Information), the charge neutrality point (CNP) voltage (V_D) of graphene on MoS_2 was estimated to be about –0.9 V based on the approximate symmetry of the spectra evolution with respect to the electron and hole doping away from this voltage.[36] The non-zero V_D could be attributed to the unintentional extrinsic doping from substrates or the environment. The doping dependence of the G bands in graphene was in good agreement with previous reports.[36,37,42] According to the Raman G mode shifts at different gate biases,[29,36,37] the carrier density of graphene was determined, and the results are presented in **Figure 4**a and Figure S2 (Supporting Information). Next, considering the electric field distribution in our devices, an applied $(V_g - V_D)$ is the sum of the potential drop across the Debye length of the electrolyte (due to the electrostatic capacitance) and the Fermi energy with respect to the CNP of the top-layer graphene (due to quantum capacitance), which can be written as[23,42]

$$\begin{aligned} e(V_{TG} - V_D) &= e^2\left(n_G + n_{MoS_2}\right)/C_{TG} + E_F(n_G), V_{TG} - V_D > 0; \\ e(V_{TG} - V_D) &= e^2\left(n_G + \Delta n_{MoS_2}\right)/C_{TG} + E_F(n_G), V_{TG} - V_D < 0; \end{aligned} \quad (4)$$

where a C_{TG} of around 2.2 μF/cm^2 is the capacitance of the gels,[40] e is the electron charge, and V_D is the Dirac point of graphene. $\Delta E_F(n_G)$ is positive for electron doping and negative for hole doping.[23] The carrier density of MoS_2 was extracted by using the above equation, and the result is presented in Figure 4a. It can be observed that the carrier density of MoS_2 can be modulated in the range from 2×10^{12} to 2.8×10^{13} cm^{-2}. According to $E_F(n_G) = hV_F\sqrt{\pi n_G}$ (for graphene, from linear E–k dispersion) and $E_F\left(n_{MoS_2}\right) = \left(\hbar\pi n_{MoS_2}/2m_e\right)e^2$ (for MoS_2), the Fermi-level shifts of graphene and MoS_2, as shown in Figure 4b, can be tuned over about 0.9 and 0.09 eV, respectively, demonstrating the significant electric-field modulation in MoS_2/graphene heterostructures.

To further demonstrate the variation in the carrier density of MoS_2, Raman spectroscopy was adopted to monitor the change of the charge state in the MoS_2 monolayer, as the peak position of the out-of-plane Raman A_{1g} mode of MoS_2 is sensitive to variations in the carrier concentration.[43,44] Figure 4c presents the Raman spectra of the MoS_2 monolayer and the corresponding peak positions ($E_{2g}{}^1$ and A_{1g} modes) at gate biases from –3.6 to 2 V. The A_{1g} mode shows a distinct blue-shift when $V_g < V_D$, whereas it shows only a slight variation when $V_g > V_D$. In contrast, the $E_{2g}{}^1$ is insensitive to the gate bias. According to the above experimental results, we interpret the data using schematic band-structure diagrams, as shown in Figure 4d. When $V_g > V_D$, an accumulation of positive ions in the electrolyte results in n-doped graphene, whereas the accumulation of negative ions at $V_g < V_D$, results in p-doped graphene. The top graphene and bottom MoS_2 feel different electric fields due to the electronic screening by the charge carriers and the dielectric constant of graphene. This electric screening will be discussed further on. The electric field from the ion-gels induces a variation in the carrier density of both graphene and MoS_2.

It needs to be further clarified whether the carrier density of MoS_2 is the sole factor determining the PL tuning in the MoS_2/graphene heterostructures. If it is, the trion intensity (I_{A^-}) should remain almost constant regardless of whether a negative or positive gate bias is applied, as has been described in previous reports.[9,10,38] In this case, a unique situation, where excess electrons are not effective in screening, can enable the trions to be stable.[45] However, in our experiments, the change in the trion intensity, as shown in Figure 3d, is different from that in previous reports after measurements of more than 8 samples.[9,10,38] As shown in Figure 3d, the trion intensity remains almost

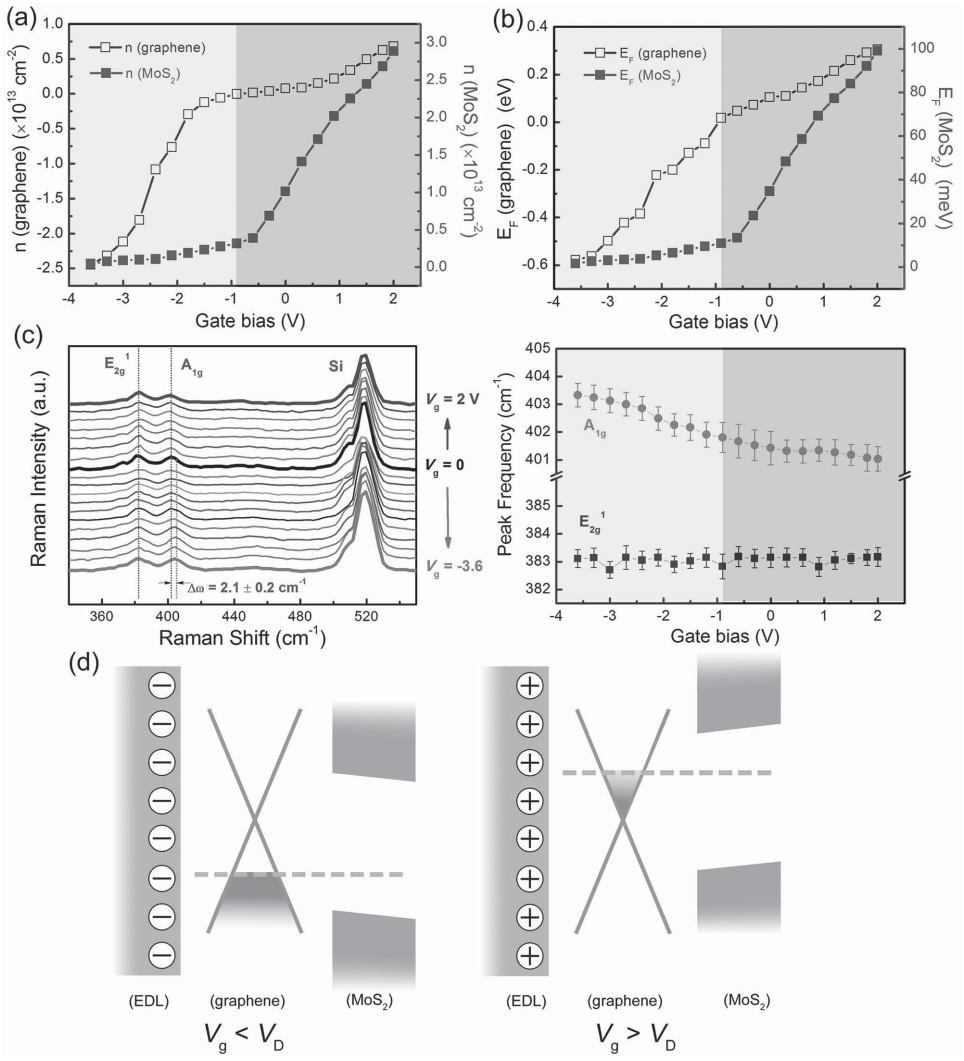

Figure 4. a) $n_{(MoS2)}$ and $n_{(graphene)}$ versus the gate bias V_g obtained as the difference between the total density and $n_{(graphene)}$. For $V_g > V_D$, the carrier density of MoS_2 increases, whereas it decreases when $V_g < V_D$. b) The Fermi level shifts of graphene and MoS_2 versus the gate bias Vg. c) The Raman spectra and corresponding Raman peak (E_{2g}^1 and A_{1g}) positions of MoS_2 at different gate bias V_g. d) Schematic band alignment of the MoS_2/graphene heterostructures for $V_g < V_D$ (p-doped graphene) and $V_g > V_D$ (n-doped graphene).

constant at negative gate bias, whereas it decreases significantly at positive gate bias. This indicates that at negative gate bias, the carrier density in MoS_2 predominantly determined the modulation of the PL, whereas at positive gate bias, the carrier density may not have major contributions to the PL tuning.

Next, we try to evaluate the effect of the band alignment at the interface between graphene and MoS_2 on the photoluminescence properties of the MoS_2/graphene heterostructures. As demonstrated by previous results,[29,30,34] the built-in electric field induced by the barrier at the interface in graphene/TMDs heterostructures can induce the separation of photogenerated electron–hole pairs, decrease the recombination efficiency, and thus lower the photoluminescence intensity. The Schottky barrier between MoS_2 and graphene at different electric fields was calculated by first-principle calculations, and the results are presented in Figure S3 (Supporting Information). Both the energetic band structures of graphene and MoS_2 preserve their pristine profiles, except that the Fermi level of graphene is shifted by the external electric field. When $V_g < V_D$, the Schottky barrier height increased, and the photogenerated holes transferred from the valence band of MoS_2 to graphene, leading to the splitting of excitons. This process is expected to decrease the PL intensity. However, as shown in Figure 2a, the PL intensity increased with increasing negative bias, indicating that the decrease in electron density (relative *p*-doping with respect to pristine MoS_2) played a dominant role. On the other hand, when $V_g > V_D$, the decreased barrier should decrease the splitting of excitons, leading to a higher PL intensity. However, the measured PL intensity in MoS_2/graphene decreased at positive gate bias. The expected results are thus inconsistent with our experimental results in Figure 2, therefore, we can speculate that the Schottky barrier is not a major factor in the PL tuning.

According to the analysis aforementioned, from the viewpoint of the heterostructural construction, there are two main factors that co-determine the photoluminescence behavior

in MoS_2/graphene heterostructures, namely the carrier density of MoS_2 and the hetero-interface.[19,29–31] At negative gate biases, the carrier density in MoS_2 plays a dominant role in the photoluminescence behavior, and the change in the trion intensity is consistent with previous reports.[9,10,38] However, at positive gate biases, the PL intensity presented a distinct quenching phenomenon. Considering the significant dependence of the trion intensity on the positive gate bias, we speculated that this quenching behavior did not result from the n-doping of MoS_2, but rather from the interlayer relaxation of the excitons.[19,29,31] In other words, at positive gate bias, the interlayer relaxation of excitons at the hetero-interface played a dominant role in the PL tuning, whereas at negative gate bias, the carrier density in the MoS_2 made a major contribution.

In order to further verify our speculation that the interlayer relaxation of excitons at the hetero-interface and the carrier density of MoS_2 co-determine the PL tuning in MoS_2/graphene heterostructures, we introduced insulated self-assembled monolayers with different thicknesses (octyltrichlorosilane C8-OTS, ca. 0.8 nm, and trichlorooctadecylsilane C18-OTS, ca. 1.8 nm) to modulate both the electric-field distribution on MoS_2/graphene and the tunneling barrier between MoS_2 and graphene. The AFM topographies shown in Figure S5 (Supporting Information) demonstrate the successful formation of the SAMs on the surface of MoS_2. To further verify the barrier between the MoS_2 monolayer and the SAMs, conductive AFM (C-AFM) measurements were carried out using a Pt/MoS_2/SAMs/tip configuration. **Figure 5**a shows the schematic illustration of the C-AFM measurements for MoS_2 or MoS_2/SAMs on Pt substrates. The AFM conductive tip (Co/Cr tip) was grounded, and the bias was applied to the samples. Figure 5b shows the *I-V* curves of Pt/MoS_2, Pt/MoS_2/C8-OTS, and Pt/MoS_2/C18-OTS. Compared to pristine MoS_2/Pt, the insertion of an insulated SAM led to a decrease in the tunneling current. Moreover, for the MoS_2/C18-OTS with a thicker insulated layer, the current is lowest. Subsequently, we used the Fowler–Nordheim (F–N) tunneling theory to analyze the *I–V* data, which can be expressed as[46,47]

$$I(V) = \frac{A_{\text{eff}} q^3 m V^2}{8\pi h \phi_B d^2 m^*} \exp\left[\frac{-8\pi\sqrt{2m^*}\,\phi_B^{\frac{3}{2}} d}{3hqV}\right] \quad (5)$$

where A_{eff} and ϕ_B are the effective contact area and the barrier height, respectively. q, m, m^*, d, and h represent the electron charge, free electron mass, effective electron mass separation between the two electrodes, and the Plank constant, respectively. The above equation can be expressed as

$$\ln\frac{I(V)}{V^2} = \ln\frac{A_{\text{eff}} q^3 m}{8\pi h \phi_B d^2 m^*} - \frac{-8\pi\sqrt{2m^*}\,\phi_B^{\frac{3}{2}} d}{3hqV} \quad (6)$$

where $m/m^* = 1.9$.[48] From the inset in Figure 5b, it can be seen that $\ln(I/V^2)$ versus $1/V$ presents a strong linear dependence, which can be fitted by the above equation, indicating that the tunneling can be explained by the F–N tunneling model. From the slope of each curve, tunneling barrier heights (ϕ_B) of 0.237 and 1.39 eV were obtained for MoS_2/C8-OTS and MoS_2/C18-OTS, respectively.

Combining this with the above results and considering the semi-metal character of graphene, we speculated that for MoS_2/SAMs/graphene, the insertion of SAMs could also increase the tunneling barrier between MoS_2 and graphene, and further impede the splitting of excitons. On the other hand, the SAMs may affect the electric screening effect (or the electric displacement distribution) across the MoS_2/SAMs/graphene structure. Thus, we measured the PL properties of these MoS_2/SAMs/graphene heterostructures, in order to verify the effect of electric screening on the carrier density of MoS_2 and the resultant excitonic states. **Figure 6**a,b shows the PL spectra of MoS_2/C8-OTS/graphene and MoS_2/C18-OTS/graphene heterostructures at gate

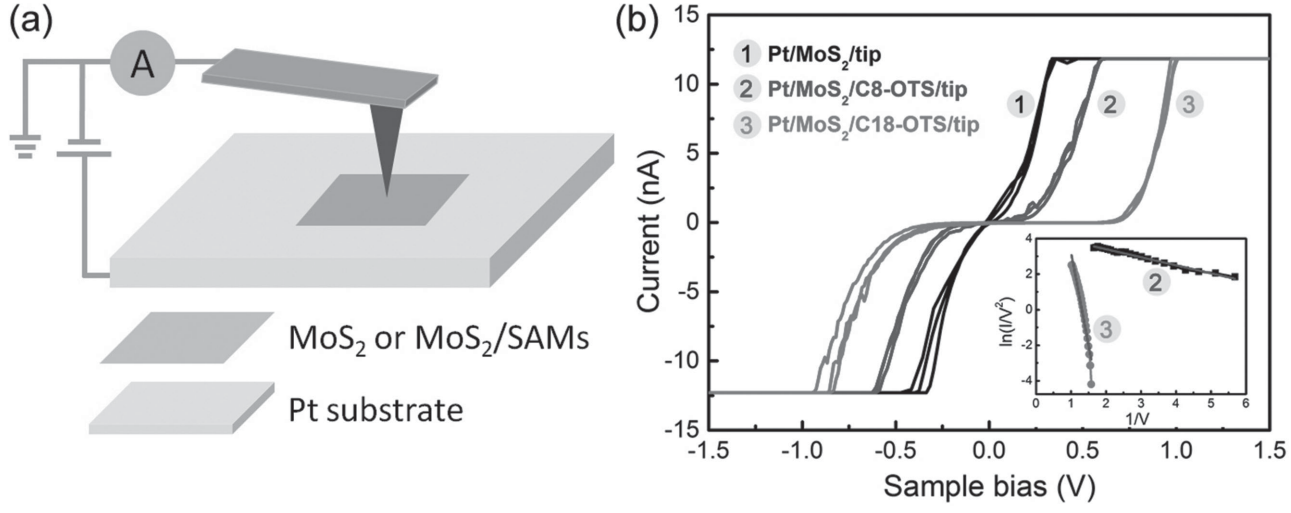

Figure 5. a) Schematic illustration of conductive atomic force microscopy (C-AFM) measurements for MoS_2 or SAMs/MoS_2 on Pt substrates. AFM tips with Co/Cr coating were used. b) *I–V* curves of Pt/MoS_2/tip, Pt/MoS_2/C8-OTS/tip, and Pt/MoS_2/C18-OTS/tip, respectively. The inset shows the fitted curves ($\ln(I/V^2)$ versus $1/V$)) calculated using the F–N tunneling model.

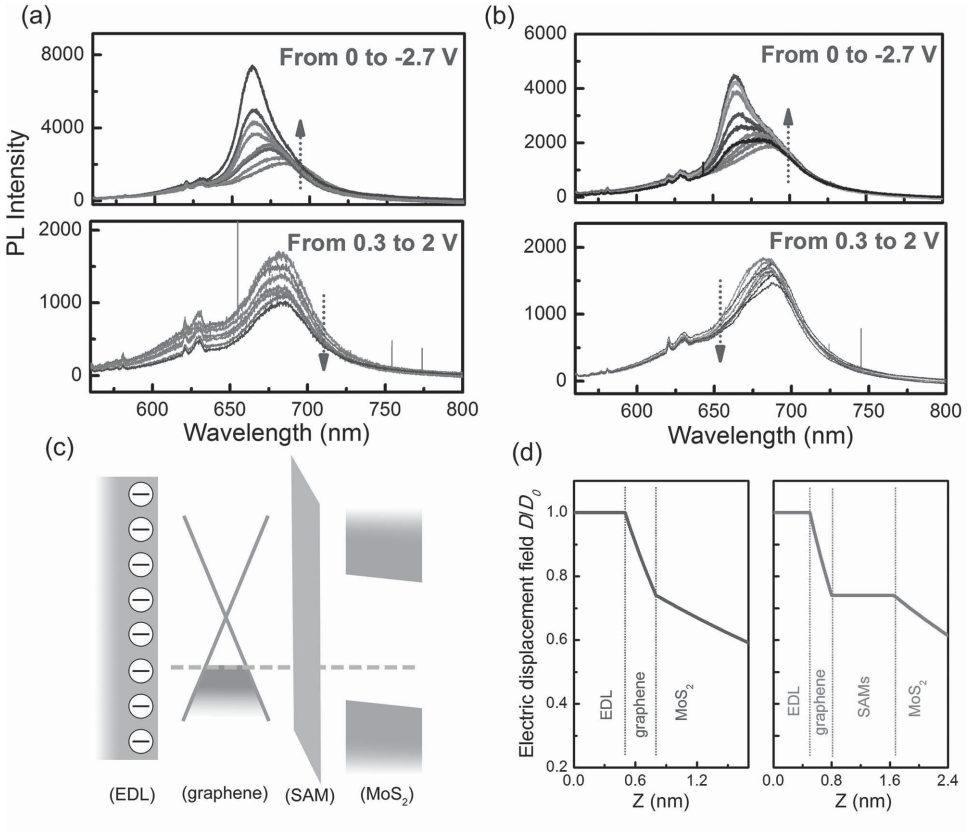

Figure 6. a,b) PL spectra of MoS_2/C8-OTS/graphene and MoS_2/C18-OTS/graphene, respectively, at gate bias from –2.7 to 2 V. c) The band alignment of MoS_2/SAMs/graphene heterostructures at negative gate bias ($V_g < V_D$), and the electric displacement field profile of the electrolyte gated for MoS_2/graphene and MoS_2/SAMs/graphene. The displacement field presents an exponential decrease as a function of Z displacement.

biases from –2.7 to 2 V. It can be observed that with increasing negative gate bias, in both cases the PL intensity increased, and the PL peak was blue-shifted, similar to the case of the MoS_2/graphene heterostructure, whereas the PL intensity decreased slightly with increasing positive gate bias, which was significantly different from the MoS_2/graphene case. Using Lorentz fitting, the peak positions and intensities of the A and B excitons, and the A^- trion could be carried out and are presented in Figures S7 and S9 in the Supporting Information. The trion intensities in both cases presented slight variations, and the exciton intensities decreased by increasing the gate bias from –2.7 to 2 V. This indicates that the variation in the carrier density of MoS_2 is the sole factor for determining the PL tuning in MoS_2/SAMs/graphene heterostructures.[9,10,38] The increase in the tunneling barrier between MoS_2 and graphene by inserting an insulated SAM significantly impedes the interlayer relaxation of the excitons, and the significant PL quenching is not observed at positive gate biases. Next, we turned our attention to the dependence of the PL intensity of MoS_2/SAMs/graphene on the gate bias as shown in Figure 6a,b. We observed that at negative gate bias the absolute PL intensities in MoS_2/C8-OTS/graphene and MoS_2/C18-OTS/graphene increased only by 3.5 and 2 times, respectively, which was much lower than that in MoS_2/graphene. Moreover, at positive gate bias, the PL intensity in the MoS_2/C8-OTS/graphene structure decreased a little faster than that in the MoS_2/C18-OTS/graphene structure.

To extract the carrier density of MoS_2 from the MoS_2/SAMs/graphene, we firstly analyzed the electric-field screening effects of graphene itself, of the insulated self-assembled monolayers, and of MoS_2, assuming that the in-plane electric field was uniform. Indeed, the electronic screening played a crucial role in creating a charge-density asymmetry in graphene and MoS_2. The relation between the electric potential $\phi(z)$ and net charge density $\rho(z)$ across the electric double layer (EDL) and channel can be determined by the Poisson equation

$$\nabla^2\phi(z) = -\frac{1}{\varepsilon_r,\varepsilon_0}\rho(z) \tag{7}$$

which was described by Zhou et al.[49] By using the Taylor expansion, the potential $\phi(z)$ shows an exponential decay: $\phi(z) = \phi_0 \exp(-z/L_D)$ in both graphene and MoS_2, where L_D is the screening length of the materials. The screening length of graphene has been reported to be 1 nm, whereas that of MoS_2 has been estimated to be about 6–10 nm.[41,50–52]

The band alignment of MoS_2/SAMs/graphene at negative gate bias is presented in Figure 6c. Figure 6d shows the electric displacement field D across the ion-gel and MoS_2/graphene (or MoS_2/SAMs/graphene), where D_0 is the electric displacement field at the electric double layer. The thickness of the electric double layer was about 0.5 nm. The electric displacement field can be assumed to be constant across the SAMs. The dielectric

constants used for graphene, SAMs, and MoS_2 were 3, 2.5, and 4, respectively.[41,53]

Note that D_0 was different in the two cases. Assuming that the same gate bias (V_g) was applied across the ion-gel and the channel, that is $\int E\,dz = V_g$, where E is the electric field determined by $\varepsilon_r\varepsilon_0 E = D$, D_0 can be determined by using the above boundary conditions. The total increase in the 2D free-carrier density in each material can then be determined from Gauss' law. And the results are as follows: $n_{(MoS_2)} = 1.355n_0$ (for MoS_2/C8-OTS/graphene) and $n_{(MoS_2)} = 1.555n_0$ (for MoS_2/C18-OTS/graphene), where n_0 is the carrier (electrons) density of MoS_2 in MoS_2/graphene. Moreover, the dependence of the electron density of MoS_2 on the gate bias in MoS_2/SAMs/graphene is quantitatively presented in Figure S11 (Supporting Information). Compared to the pristine MoS_2/graphene structure, the insertion of a SAM weakens the electric field tuning on the carrier density of MoS_2 in MoS_2/SAMs/graphene heterostructures.

3. Conclusions

We have studied the evolution of excitonic states in MoS_2/graphene and MoS_2/SAMs/graphene heterostructures by electrochemical gating, and found that the PL intensity of the excitons (or trions) could be modulated by more than two orders of magnitude and the trion/exciton intensity ratio in MoS_2/graphene could be changed by up to 30 times. By extracting the carrier densities of the counterparts using an electric potential distribution model and the contact barrier at the hetero-interface by first-principle calculations, we could deduce that at negative gate bias the variation in carrier density of MoS_2 had a major contribution to the PL tuning, whereas at positive gate bias the interlayer relaxation of excitons at the hetero-interface played a dominant role. This was further verified by controlling the tunneling barrier at the interface and electric field across MoS_2/graphene by introducing insulated SAMs with different thicknesses. Our results demonstrate the significance of many-body interactions and a hetero-interface for tuning the optical and optoelectronic performance of vdWs heterostructures.

4. Experimental Section

Preparation of MoS_2/Graphene Heterostructures Devices: Monolayer and bilayer MoS_2 nanoflakes were mechanically exfoliated onto a Si/SiO_2 wafer and identified by optical microscopy. Monolayers of graphene was synthesized by a CVD method according to previous reports.[54] Graphene on a Cu foil was covered with PMMA (950 PMMA, Sigma-Aldrich) by spin coating (3000 rpm for 1 min), and baked at 135 °C for 15 min. Then, the Cu foil was etched by a mixed solution (6 M HCl and 1 M $FeCl_3$) in water. After rigorous cleaning, the graphene was transferred onto the Si/SiO_2 wafer with monolayer or bilayer MoS_2 nanoflakes, followed by the removal of PMMA with acetone for 6 h. The Cr/Au electrodes with a thickness of 5/100 nm were deposited by thermal evaporation using metal shadow masks.

Electrolyte Preparation: The electrolyte was prepared by dissolving lithium perchlorate ($LiClO_4$) and polyethylene oxide (PEO) in methane at a ratio of 0.012:0.1:4 under stirring at 45 °C. A droplet was then deposited onto the device and left to dry.

Preparation of MoS_2/SAMs/Graphene Heterostructures: Two kinds of silanes (octyltrichlorosilane C8-OTS, and trichlorooctadecylsilane C18-OTS) were purchased from Sigma-Aldrich. For the formation of OTS SAMs, the substrates were immersed into the silane/n-hexane solution (1:100 v:v) for 2–4 h. After film deposition, the substrates were subsequently washed with toluene, acetone, and alcohol, for several times, and then baked at 120 °C for 20 min. The CVD-graphene on Cu foil was transferred to the OTS modified MoS_2 substrates by the transfer method described above.

Preparation of Pt/MoS_2/SAMs: The MoS_2 monolayer was transferred to the Si/SiO_2/Ti/Pt substrates by using a wet transfer method. Then, the substrates were immersed into the OTS solutions (OTS/n-hexane 100uL/10 mL) for 2–4 hours to allow the formation of OTS SAMs. After film deposition, the substrates were successively washed with toluene, acetone, and alcohol for several times and then baked at 120 ºC for 20 min.

Raman and PL Measurements: The gate bias was applied to the gels using a Keithley 2420, and the PL and Raman spectra (LabRAM ploRA, incident power of less than 0.5 mW, pumping wavelength of 532 and 618 nm, integral time of 10 s for PL, 30 s for Raman) were measured after the charge was stable 15 to 25 min later.

AFM, Kelvin Probe Microscopy (KFM), *and conductive AFM Measurements*: The AFM topography, KFM, and conductive AFM measurements were conducted using a Bruker Dimension ICON-PT with Co/Cr tips. The principle of KFM has been described in previous reports.[43,50] For conductive AFM measurements, the Co/Cr tip was grounded, and the bias was applied to the samples, moreover, the contact force was kept at 25 to 30 nN to maintain a good reproducibility.

Supporting Information

Supporting Information is available from the Wiley Online Library or from the author.

Acknowledgements

This work was financially supported by the National Natural Science Foundation of China (No. 51572057), the State Key Laboratory of Advanced Welding and Joining (AWJ-M15-11), the National Basic Research Program of China (2012CB934102), the Ministry of Science and Technology of China (2012AA030303), and the Fundamental Research Funds for the Central Universities (HIT.BRETIII.201203). Y.L. and L.Z. also acknowledge the support from the Lam Research Corp.

Received: July 28, 2015
Revised: September 28, 2015
Published online: November 20, 2015

[1] A. Splendiani, L. Sun, Y. Zhang, T. Li, J. Kim, C. Y. Chim, G. Galli, F. Wang, *Nano Lett.* **2010**, *10*, 1271.
[2] Q. H. Wang, K. Kalantar-Zadeh, A. Kis, J. N. Coleman, M. S. Strano, *Nat. Nanotechnol.* **2012**, *7*, 699.
[3] O. Lopez-Sanchez, D. Lembke, M. Kayci, A. Radenovic, A. Kis, *Nat. Nanotechnol.* **2013**, *8*, 497.
[4] J. Wilson, A. Yoffe, *Adv. Phys.* **1969**, *18*, 193.
[5] K. F. Mak, C. Lee, J. Hone, J. Shan, T. F. Heinz, *Phys. Rev. Lett.* **2010**, *105*, 136805.
[6] D. Xiao, G. B. Liu, W. Feng, X. Xu, W. Yao, *Phys. Rev. Lett.* **2012**, *108*, 196802.
[7] B. Zhu, H. Zeng, J. Dai, X. Cui, *Adv. Mater.* **2014**, *26*, 5504.
[8] C.-H. Chen, C.-L. Wu, J. Pu, M.-H. Chiu, P. Kumar, T. Takenobu, L.-J. Li, *2D Materials* **2014**, *1*, 034001.
[9] K. F. Mak, K. He, C. Lee, G. H. Lee, J. Hone, T. F. Heinz, J. Shan, *Nat. Mater.* **2013**, *12*, 207.
[10] S. Mouri, Y. Miyauchi, K. Matsuda, *Nano Lett.* **2013**, *13*, 5944.

[11] J. S. Ross, S. Wu, H. Yu, N. J. Ghimire, A. M. Jones, G. Aivazian, J. Yan, D. G. Mandrus, D. Xiao, W. Yao, X. Xu, *Nat. Commun.* **2013**, *4*, 1474.
[12] A. M. Jones, H. Yu, N. J. Ghimire, S. Wu, G. Aivazian, J. S. Ross, B. Zhao, J. Yan, D. G. Mandrus, D. Xiao, *Nat. Nanotechnol.* **2013**, *8*, 634.
[13] A. Castellanos-Gomez, R. Roldan, E. Cappelluti, M. Buscema, F. Guinea, H. S. van der Zant, G. A. Steele, *Nano Lett.* **2013**, *13*, 5361.
[14] K. He, C. Poole, K. F. Mak, J. Shan, *Nano Lett.* **2013**, *13*, 2931.
[15] H. J. Conley, B. Wang, J. I. Ziegler, R. F. HaglundJr., S. T. Pantelides, K. I. Bolotin, *Nano Lett.* **2013**, *13*, 3626.
[16] Y. Lin, X. Ling, L. Yu, S. Huang, A. L. Hsu, Y.-H. Lee, J. Kong, M. S. Dresselhaus, T. Palacios, *Nano Lett.* **2014**, *14*, 5569.
[17] A. K. Geim, I. V. Grigorieva, *Nature* **2013**, *499*, 419.
[18] L. Britnell, R. Ribeiro, A. Eckmann, R. Jalil, B. Belle, A. Mishchenko, Y.-J. Kim, R. Gorbachev, T. Georgiou, S. Morozov, *Science* **2013**, *340*, 1311.
[19] X. Hong, J. Kim, S. F. Shi, Y. Zhang, C. Jin, Y. Sun, S. Tongay, J. Wu, F. Wang, *Nat. Nanotechnol.* **2014**, *9*, 682.
[20] K. Roy, M. Padmanabhan, S. Goswami, T. P. Sai, G. Ramalingam, S. Raghavan, A. Ghosh, *Nat. Nanotechnol.* **2013**, *8*, 826.
[21] H. Fang, C. Battaglia, C. Carraro, S. Nemsak, B. Ozdol, J. S. Kang, H. A. Bechtel, S. B. Desai, F. Kronast, A. A. Unal, G. Conti, C. Conlon, G. K. Palsson, M. C. Martin, A. M. Minor, C. S. Fadley, E. Yablonovitch, R. Maboudian, A. Javey, *Proc. Natl. Acad. Sci. USA* **2014**, *111*, 6198.
[22] C.-H. Lee, G.-H. Lee, A. M. van Der Zande, W. Chen, Y. Li, M. Han, X. Cui, G. Arefe, C. Nuckolls, T. F. Heinz, *Nat. Nanotechnol.* **2014**, *9*, 676.
[23] S. Larentis, J. R. Tolsma, B. Fallahazad, D. C. Dillen, K. Kim, A. H. MacDonald, E. Tutuc, *Nano Lett.* **2014**, *14*, 2039.
[24] M.-H. Chiu, C. Zhang, H.-W. Shiu, C.-P. Chuu, C.-H. Chen, C.-Y. S. Chang, C.-H. Chen, M.-Y. Chou, C.-K. Shih, L.-J. Li, *Nat. Commun.* **2015**, *6*, 7666.
[25] J. Y. Kwak, J. Hwang, B. Calderon, H. Alsalman, N. Munoz, B. Schutter, M. G. Spencer, *Nano Lett.* **2014**, *14*, 4511.
[26] H.-P. Komsa, A. V. Krasheninnikov, *Phys. Rev. B* **2013**, *88*, 085318.
[27] K. Liu, L. Zhang, T. Cao, C. Jin, D. Qiu, Q. Zhou, A. Zettl, P. Yang, S. G. Louie, F. Wang, *Nat. Commun.* **2014**, *5*, 4966.
[28] S. Huang, X. Ling, L. Liang, J. Kong, H. Terrones, V. Meunier, M. S. Dresselhaus, *Nano Lett.* **2014**, *14*, 5500.
[29] C.-J. Shih, Q. H. Wang, Y. Son, Z. Jin, D. Blankschtein, M. S. Strano, *ACS Nano* **2014**, *8*, 5790.
[30] M. Bernardi, M. Palummo, J. C. Grossman, *Nano Lett.* **2013**, *13*, 3664.
[31] Y. Yu, S. Hu, L. Su, L. Huang, Y. Liu, Z. Jin, A. A. Purezky, D. B. Geohegan, K. W. Kim, Y. Zhang, *Nano Lett.* **2014**, *15*, 486.
[32] P. Rivera, J. R. Schaibley, A. M. Jones, J. S. Ross, S. Wu, G. Aivazian, P. Klement, K. Seyler, G. Clark, N. J. Ghimire, *Nat. Commun.* **2015**, *6*, 6242.
[33] F. Ceballos, M. Z. Bellus, H.-Y. Chiu, H. Zhao, *ACS Nano* **2014**, *8*, 12717.
[34] J. He, N. Kumar, M. Z. Bellus, H.-Y. Chiu, D. He, Y. Wang, H. Zhao, *Nat. Commun.* **2014**, *5*, 5622.
[35] H. Coy Diaz, J. Avila, C. Chen, R. Addou, M. C. Asensio, M. Batzill, *Nano Lett.* **2015**, *15*, 1135.
[36] A. Das, S. Pisana, B. Chakraborty, S. Piscanec, S. Saha, U. Waghmare, K. Novoselov, H. Krishnamurthy, A. Geim, A. Ferrari, *Nat. Nanotechnol.* **2008**, *3*, 210.
[37] J. Liu, Q. Li, Y. Zou, Q. Qian, Y. Jin, G. Li, K. Jiang, S. Fan, *Nano Lett.* **2013**, *13*, 6170.
[38] P. T. K. Loan, W. Zhang, C. T. Lin, K. H. Wei, L. J. Li, C. H. Chen, *Adv. Mater.* **2014**, *26*, 4838.
[39] W. Zhang, C.-P. Chuu, J.-K. Huang, C.-H. Chen, M.-L. Tsai, Y.-H. Chang, C.-T. Liang, H. He Jr., M.-Y. Chou, L.-J. Li, *Sci. Rep.* **2014**, *4*, 3826.
[40] J. Siviniant, D. Scalbert, A. Kavokin, D. Coquillat, J. Lascaray, *Phys. Rev. B* **1999**, *59*, 1602.
[41] E. J. Santos, E. Kaxiras, *ACS Nano* **2013**, *7*, 10741.
[42] T.-F. Chung, R. He, T.-L. Wu, Y. P. Chen, *Nano Lett.* **2015**, *15*, 1203.
[43] Y. Li, C.-Y. Xu, P. Hu, L. Zhen, *ACS Nano* **2013**, *7*, 7795.
[44] B. Chakraborty, A. Bera, D. Muthu, S. Bhowmick, U. Waghmare, A. Sood, *Phys. Rev. B* **2012**, *85*, 161403.
[45] G. Finkelstein, H. Shtrikman, I. Bar-Joseph, *Phys. Rev. Lett.* **1995**, *74*, 976.
[46] A. Olbrich, B. Ebersberger, C. Boit, *Appl. Phys. Lett.* **1998**, *73*, 3114.
[47] G. H. Lee, Y. J. Yu, C. Lee, C. Dean, K. L. Shepard, P. Kim, J. Hone, *Appl. Phys. Lett.* **2011**, *99*, 243114.
[48] Y. Yoon, K. Ganapathi, S. Salahuddin, *Nano Lett.* **2011**, *11*, 3768.
[49] Y. Zhou, J. Park, J. Shi, M. Chhowalla, H. Park, D. A. Weitz, S. Ramanathan, *Nano Lett.* **2015**, *15*, 1627.
[50] Y. Li, C.-Y. Xu, L. Zhen, *Appl. Phys. Lett.* **2013**, *102*, 143110.
[51] S. Das, J. Appenzeller, *Phys. Status Solidi (RRL)* **2013**, *7*, 268.
[52] E. J. Santos, E. Kaxiras, *ACS Nano* **2013**, *7*, 10741.
[53] S. A. DiBenedetto, A. Facchetti, M. A. Ratner, T. J. Marks, *Adv. Mater.* **2009**, *21*, 1407.
[54] T. Ma, W. Ren, Z. Liu, L. Huang, L.-P. Ma, X. Ma, Z. Zhang, L.-M. Peng, H.-M. Cheng, *ACS Nano* **2014**, *8*, 12806.